

Transformation of the singular skeleton in optical-vortex beams diffracted by a rectilinear phase step

Aleksandr Bekshaev^{1*}, Anna Khoroshun², Lidiya Mikhaylovskaya¹

¹*Odessa I.I. Mechnikov National University, Dvorianska 2, 65082 Odessa, Ukraine*

²*V. Dahl East Ukrainian National University, Pr. Central, 59-A, 93400 Severodonetsk, Ukraine*

^{*}*Corresponding author: bekshaev@onu.edu.ua*

Based on the Kirchhoff-Fresnel approximation, we numerically analyze spatial characteristics of the light field formed after a circular Laguerre-Gaussian beam with a single-charged optical vortex (OV) passes the transparent screen with a rectilinear phase step. The main attention is paid to the localization and interactions of the OVs, which form the singular skeleton of the transformed field. The phase-step influence depends on its value and position with respect to the beam axis. Upon “weak perturbation” (low phase step) the main effect is that the OV is shifted from the initial axial position and describes a closed loop when the phase step is monotonously translated across the beam. The “strong perturbation” (the phase step is close to π) induces discontinuities in the OV trajectories (“jumps”) and emergence of additional singularities in the near-axial region of the beam cross section. The details of the OV migration and singular skeleton transformations reveal the fundamental helical nature and transverse energy circulation in the OV beams. The numerical results obtained in this paper show the possibilities for the purposeful control of the singular skeleton characteristics within the transformed beam, and can be useful for the OV diagnostics, OV metrology and micromanipulation techniques.

Keywords: optical vortex; Laguerre-Gaussian beam; phase step; diffraction; transverse beam profile; singular skeleton; topological reaction

PACS: 41.20.-q; 42.25.Fx; 42.60.Jf; 42.50.Tx

OCIS codes: 050.4865 (Optical vortices); 050.1940 (Diffraction); 140.3300 (Laser beam shaping); 070.2580 (Paraxial wave optics); 260.6042 (Singular optics)

1. Introduction

The study of structured optical fields, in particular, those with optical vortices (OV), is one of the prospective lines of modern optics [1–4]. In scalar paraxial beams, an OV is formed near an isolated point (phase singularity, OV core) with zero amplitude and indeterminate phase of the optical field. The field behavior in the nearest vicinity of the phase singularity is rather standard: the equal-amplitude lines are ellipses centered at the OV core, and upon a round trip near this point, the field phase changes by $2\pi m$ (the integer m is the OV topological charge). The phase singularity is associated with the screw wavefront dislocation and is a center of the transverse energy circulation being the source of the orbital angular momentum [1–5]. The set of such singularities determine the singular skeleton of the beam that qualitatively characterizes the optical field topology, which is relatively stable with respect to external perturbations. The exclusive nature of the singular points makes them well-identifiable, precisely localizable and sensitive “fingerprints” reflecting the optical field state and prehistory [6–9], which is used in numerous metrological applications [10–13]. The beams with OVs find many research and technology utilizations; particularly, they can be employed

for the controllable trapping and manipulation of micro-objects (see, e.g. [14–17]) as well as for the information encoding and processing [18,19].

For all fundamental and applied aims, the controllable formation of the OV beam singular skeleton with necessary properties is an insistent problem. It is usually solved by means of purposeful transformations performed to the standard OV beams (e.g., Laguerre-Gaussian (LG) modes [2–4]) with the help of special adjustable optical elements, which can be realized either “physically” or, very efficiently, by means of the computer-driven spatial light modulators (SLM). But prior to employ the unique SLM abilities, one must know how the modeled elements act on the standard input beam, and which modifications of the element’s parameters are desirable for obtaining the necessary singular structure at the output. In this context, the detailed studies of the OV beams’ transformations performed by various optical units, are conducted with high intensity [20–32].

It is known that the efficient control of the singular skeleton can be realized in the processes of the OV beam diffraction [21,22,27–31]. Studies of the edge diffraction of circular OV beams have demonstrated the intriguing dynamics of the phase singularities in the diffracted fields. The multicharged incident OVs (with $|m| > 1$) are decomposed into a set of $|m|$ single-charged “secondary” ones; the secondary OVs evolve along intricate spiral-like trajectories; sometimes the topological reactions occur with generation of “new” OVs and annihilation of “old” ones – in a whole, the singular skeleton of the diffracted beam forms a well developed and controllable set of OVs with the potential of being fruitfully applied in sensitive metrology and optical-trapping techniques.

However, the edge-diffraction schemes are coupled with certain limitations of the available singular skeleton transformations. It is known that the use of other diffractive elements, especially those of the pure phase nature (where the amplitude transmission is homogeneous, and only the phase of the incident beam is modulated) supply many new and potentially utilizable features [20,32–36]. In this context, the simplest phase diffractive elements with rectilinear phase step attract the especial attention. They carry distinct similarities with the well studied edge-diffraction case, and their investigation can be based on the firmly established and reliable footing. Importantly, the corresponding transformations can be easily realized by means of the usual optical elements as well as via the SLM technique. In the current literature, various aspects of the OV beam diffraction by the phase-step transparencies were analyzed [13,22,37–39], and they show promising results, first of all, for the detection of microscopic phase inhomogeneities. However, to the best of our knowledge, a systematic investigation of the OV-beam transformations induced by the phase-step diffraction elements has not been performed.

That is why in this paper we undertake such an attempt. As a generic example of the input OV beam, we consider a Laguerre-Gaussian mode LG_{pm} with zero radial index p [2–4]. This is a usual simplification rather typical for the studies of the OV beams’ transformations [23–31,34,36]. But if the incident LG beam is multicharged ($|m| > 1$), the multiple “secondary” OVs separately evolve in the diffracted beam. As a result, specific details of their behavior, although interesting and informative [29–31,38], generally, “mask” the main physical features of the diffracted field associated with the screw wavefront dislocation and the circular energy flow in the incident OV beam. Therefore, in this study we make an additional simplification and restrict ourselves to the case of single-charged incident beam ($|m| = 1$): this not only facilitates the analysis and calculations but promotes to unveiling the generic features of the OV transformations by a phase-step screen.

In the subsequent sections, our main interest concerns the OV displacements, induced by the phase-step transformation, and their migration over the diffracted beam cross section when the phase-step transparency moves across the incident OV beam. Depending on the phase-step “height” and the propagation distance behind the screen, the cases of “weak” and “strong” perturbation are distinguished. In the latter case, the topological reactions and formation of fully developed singular-skeleton structure are described and discussed. The main regularities of the OV migration in

different diffracted beam cross sections, including the far field (Fraunhofer diffraction), are examined. The final results open new possibilities for the singular skeleton regulation and show additional ways for the physical characterization and diagnostics of the OV beams. Their potential impact and possible applications are briefly outlined in the Conclusion. The whole presentation is based on the numerical analysis but is confirmed by the asymptotic analytical description of the OV migration in the diffracted beam cross section presented in Appendix.

2. Description of the phase-step diffraction model

The general scheme of the incident beam transformation is presented in figure 1 [28–31]. The incident monochromatic paraxial beam propagates along axis z , and the spatial distribution of its electric field is described by the function $\text{Re}[u(x, y, z) \exp(ikz - i\omega t)]$ where $\omega = ck$, c is the velocity of light, k is the wavevector related with the wavelength λ as $k = 2\pi/\lambda$, and $u(x, y, z)$ is the slowly varying complex amplitude [3,5]. In the plane $z = 0$, the amplitude-phase corrector (screen) is situated with variable and, generally, adjustable transparency; in further references we call this plane “screen plane”, or “initial plane”. To highlight this plane, the transverse Cartesian frame at $z = 0$ is furnished with special notations (x_a, y_a) , and the incident complex amplitude is denoted as $u_a(x_a, y_a)$; then, the transformation performed by the screen is described by the equation

$$u_a(x_a, y_a) \rightarrow T(x_a, y_a) u_a(x_a, y_a). \quad (1)$$

In this paper, we consider the corrector consisting of two parts with different transmittances, divided by the line $x_a = a$ (see figure 1):

$$T(x_a, y_a) = \begin{cases} A, & x_a < a; \\ B, & x_a \geq a. \end{cases} \quad (2)$$

In particular, (2) describes the usual edge diffraction if one part of the screen is opaque (see, e.g., Refs. [26–31] where the situation corresponds to $A = 1$, $B = 0$). Now we analyze the problem in which the screen is homogeneously transparent, $|T(x_a, y_a)| = 1$, but contains a phase step: for $x < a$ the transmission is still $T(x_a, y_a) = 1$ while for $x > a$, a certain coordinate-independent phase φ is added to the light field:

$$A = 1, \quad B = \exp(i\varphi). \quad (3)$$

In figure 1, the phase step in the form of two joint glass plates of different thicknesses is shown for illustrative purposes; in reality, the phase step can be realized by any other means, e.g., with the SLM or a liquid crystal cell.

The complex amplitude $u(x, y, z, a)$ of the propagating diffracted beam in the observation plane positioned at a distance z behind the screen with the phase step located at $x_a = a$ can be found via the Kirchhoff-Fresnel integral [29,31,40,41]

$$\begin{aligned} u(x, y, z, a) &= \frac{k}{2\pi iz} \int_{-\infty}^{\infty} dy_a \int_{-\infty}^{\infty} dx_a T(x_a, y_a) u_a(x_a, y_a) \exp\left\{\frac{ik}{2z}[(x - x_a)^2 + (y - y_a)^2]\right\} \\ &= \frac{k}{2\pi iz} \int_{-\infty}^{\infty} dy_a \int_{-\infty}^a dx_a u_a(x_a, y_a) \exp\left\{\frac{ik}{2z}[(x - x_a)^2 + (y - y_a)^2]\right\} \\ &\quad + \frac{k}{2\pi iz} \exp(i\varphi) \int_{-\infty}^{\infty} dy_a \int_a^{\infty} dx_a u_a(x_a, y_a) \exp\left\{\frac{ik}{2z}[(x - x_a)^2 + (y - y_a)^2]\right\}. \end{aligned} \quad (4)$$

Our task is to study the optical field formed behind the transparency (2), (3) when the incident field is a circular beam with OV. As was explained in the Introduction, a generic example of such beams

is provided by the LG_{0m} -beam with zero radial index and, to avoid unnecessary complications and to unveil the main physical features of the OV-beam diffraction associated with its helical nature, we consider the single-charged incident beam. In this case, the integral (4) can be reduced to explicit analytical expressions (see, e.g., [23,24,26]) but its numerical evaluation is also appropriate; anyway, the exact (x, y) coordinates of the OV cores are found numerically as the zeros of amplitude – solutions to the equation $u(x, y, z) = 0$ [28–31].

According to the experimental scheme of [28,29] (see figure 1), we consider the LG_{0m} incident beam with $m = -1$ (clockwise energy circulation as seen from the positive end of the z -axis, see figure 1). Additionally we suppose that the screen plane coincides with the beam's waist plane $z = 0$, that is

$$u_a(x_a, y_a) \propto \frac{x_a - iy_a}{b^2} \exp\left(\frac{x_a^2 + y_a^2}{2b^2}\right) \quad (5)$$

where b is the Gaussian envelope waist radius [2,5]. Note that if the incident complex amplitude is modified according to the equation

$$u_a(x_a, y_a) \rightarrow u_a(x_a, y_a) \exp\left(ik \frac{x_a^2 + y_a^2}{2R}\right) \quad (6)$$

(e.g., the plane wavefront is replaced by the spherical one preserving the same intensity profile), the diffracted beam pattern can, by means of the simple scaling transformation, be obtained from that derived for the initial complex amplitude $u(x_a, y_a)$ [26,30]. Therefore, despite the accepted plane-front limitation, results of the present analysis can be easily adapted to arbitrary converging or diverging beams with non-zero wavefront curvature R^{-1} in (6).

Other useful generalizations follow from the symmetry of the circular OV beams and the geometric symmetries inherent in the situation presented in figure 1. For example, the inversion of the incident OV sign ($m \rightarrow -m$) means that in the integrands of (4) $u_a(x_a, y_a) \rightarrow u_a(x_a, -y_a)$, which results in the replacement $u(x, y, z, a) \rightarrow u(x, -y, z, a)$ for the diffracted field. Therefore, for incident beams with positive OVs, all the patterns presented below in figures 2 – 5 should be mirror-reflecting with respect to the x -axis. A bit longer chain of arguments including the LG beams' property $u_a(-x_a, -y_a) = (-1)^m u_a(x_a, y_a)$ and proper inversions of signs of the integration variables in (4) leads to a conclusion that for the opposite phase step, $\varphi \rightarrow -\varphi$, the output beam complex amplitude can be obtained from the result of (4) through the transformation

$$u(x, y, z, a) \rightarrow e^{-i\varphi} (-1)^m u(-x, -y, z, -a). \quad (7)$$

This permits us to consider only the case of positive φ .

For the incident beam (5), the diffraction integral (4) can be expressed via the set of dimensionless spatial parameters where all the transverse sizes (including the step position a) are expressed in units of the beam waist radius b (or its derivatives as given by equation (9) below) and all the longitudinal parameters – in units of the Rayleigh range [2,3,29]

$$z_R = kb^2. \quad (8)$$

This scaling scheme is systematically used in further presentation and exposition of the results; however, in all numerical calculations we supposed the specific conditions of Refs. [28,29] where the incident $\text{LG}_{0,-1}$ beam of the He-Ne laser radiation with parameters

$$k = 10^5 \text{ cm}^{-1}, \quad b_0 = 0.232 \text{ mm}, \quad z_R = 53.8 \text{ cm}$$

was employed.

3. Characteristics of the transformed beam and singular skeleton structures

3.1. General features of the diffracted beam profile

In this section we analyze the influence of the phase-step transparency (figure 1) on the spatial characteristics of the diffracted beam propagating behind the screen. The general illustration of the corresponding beam transformation is given in figure 2 where the diffracted beams' intensity and phase profiles are presented. The phase profiles in the right column of figure 2 are expressed by the equiphase lines of different colors: the local phase grows from violet to blue, from blue to cyan, and so on, with increment 1 rad. The complicated multiply-connected phase surfaces of the OV beams cannot be projected onto a plane without cuts which are seen as tight “bundles” of differently colored lines; ends of the cuts are just the points of phase singularities where the field amplitude is zero, i.e. the OV cores (denoted in figure 2 by V_j with $j = 1$ to 4).

1st row of figure 2 expectedly shows that the phase step $\varphi = \pi/3$ makes a weaker perturbation of the beam than the opaque-screen edge in the case of edge diffraction [20–31]: even at $a = 0$ (the phase edge crosses the beam center), the diffracted beam preserves the ring-like shape, although deformed; the main visible influence of the phase step is that the OV V_1 is shifted from the initial axial position. Case of $\varphi = \pi$ (2nd and 3rd rows of figure 2) show much higher perturbation: even when the step is positioned rather far from the center ($a = 1$ in units of b for the bottom row), the beam structure is essentially modified, which is well seen in the intensity patterns of figures 2c and 2e. Not only the axial OV is displaced (V_1 in figures 2d and 2f) but also additional OVs appear. Generally, this is not surprising: in any case of the sharp-edge diffraction, “occasional” OVs emerge at the diffracted beam periphery simultaneously with the diffraction fringes [21,22,26,27] (normally, with further post-screen propagation these OVs rapidly migrate to the periphery of the beam cross section, and they are not considered in our present context). But now, in figure 2, together with the presumably “occasional” peripheral OVs (V_3 and V_4 in figure 2d), new near-axial singularities appear (V_2 and V' in figures 2d, f): the complex singular skeleton is formed.

Figure 2 shows that the whole pattern of the diffracted beam perturbed by the rectilinear phase step is rather intricate, and its thorough study is a special task. In this paper we will concentrate on the main singular skeleton characteristics: positions of the near-axial OVs, directly associated with the OV carried by the incident beam, and their migration over the beam cross section when the phase step moves across the incident beam transverse profile.

In the calculations, we investigate the situations when the phase-step screen moves from $a = 3$ towards $a = -3$ (theoretically, from the “right infinity” ∞ to the “left infinity” $-\infty$ when seeing against the beam propagation). The figures 3 – 5 below show the migration of OVs over the beam cross section in the chosen observation planes situated at $z = 0.56z_R$ (z_R is the Rayleigh length (8)), $z = 1.5z_R$ and in the far field (Fraunhofer diffraction [40,41]). To make the data relating to different propagation distances more comparable, the transverse coordinates are expressed in units of the current Gaussian envelope radius (see (5))

$$b_c = b \sqrt{1 + \left(\frac{z}{z_R} \right)^2}. \quad (9)$$

For the far-field patterns, this normalization means that the angular far-field coordinates are expressed in units of the incident beam divergence $\gamma = (kb)^{-1}$: $(x/b_c, y/b_c) \rightarrow (x/z)kb, (y/z)kb$.

3.2. OV migration in the case of weak perturbation

In further presentation, it is convenient to classify the phase-step influences on the OV positions by two categories. In the first case, the OV core shifts from the nominal axial position and evolves along a certain smooth curve. We will refer to such situations as to the “weak perturbation” pattern, and some of them are presented in this section. In the opposing case, the diffracted beam structure is modified stronger so that the OV trajectory becomes discontinuous, the events of OV birth,

annihilation and other topological reactions take an essential place; this will be termed “strong perturbation”. Of course, this division involves not only the transparency shaping; the “strength” of the perturbation depends on the diffracted beam propagation, and sometimes the same transparency performs the strong perturbation just behind the screen ($z < z_R$) but the weak one in the far field ($z \gg z_R$). But, generally, the beams passed phase steps with $\varphi < 0.7\pi$ can be considered as weakly perturbed, and the typical situations are illustrated by figure 3. These OV trajectories qualitatively differ from the case of $\varphi = \pi$ that will be discussed further.

In figure 3 we see that initially, while $\infty > a > 2$, the only consequence of the phase-step perturbation is that the axial OV in the diffracted beam is slightly displaced from the nominal position (at the z -axis) and moves along the spiral trajectory with theoretically infinite number of coils. Note that when the phase step advances towards the axis, the spiral of the OV trajectory evolves oppositely to the energy circulation in the incident beam (cf. the arrow in figure 1). This spiral-like evolution is a consequence of the interference between the unperturbed incident beam and the edge wave generated by the sharp edge [41] (here – by the rectilinear phase step) and is similar to what was observed in the usual edge-diffracted beams [29,31]; it is well described by the asymptotic analytical model that can be derived for the case $a \gg b$ (see Appendix). In this part of the trajectory, corresponding to $\infty > a > 2$, the absolute OV displacement inversely depends on z [29–31]; that is why the segment of spiral-like OV evolution at $a > 2$ can be traced in figure 3a but becomes less perceptible in figure 3b and completely disappears in the far-field situation of figure 3c. Anyway, in such segments the OV displacements are small and of a minor practical interest, at least for the simple situation of the single-charged LG beam considered here.

With a subsequent phase-step translation, the OV deviates from the spiral trajectory (approximately when $a = 1$ in figure 3a) and moves rather far from the axis “escaping” from the approaching phase step. Expectedly, the absolute value of this deviation is higher for the higher phase steps (stronger incident beam perturbation for the same step positions). This sort of evolution continues until $a = 0$ (the phase step crosses the incident beam center), after which the OV motion is slowed down and turns back toward the axis. The “return point” occurs approximately at $a = -0.4$ for $z = 0.56z_R$, $a = -0.3$ for $z = 1.5z_R$ and exactly at $a = 0$ in the far field.

During the following screen translation towards $a = -\infty$, the OV trajectories make closed loops, ultimately returning to the nominal beam axis. It is seen that the “global” OV circulation along the whole loop is always clockwise, i.e. matches the energy circulation in the incident beam (according to relation (7), for negative φ , the same screen translation would induce a counter-clockwise OV migration). The size of the loop is higher for higher φ (cf. the green, blue and red curves in figure 3). With growing phase step, the diffracted beam perturbation becomes sufficient for inspiration of the trajectory discontinuities and associated topological reactions: in case of $\varphi = 2\pi/3$ and at small distance behind the screen (red curve in figure 3a), the OV trajectory experiences a “jump” similar to those investigated in Refs. [29–31] (in fact, this situation is “transient” to the strong-perturbation case considered below, cf. the jumps of the red and green trajectories in figure 6).

Actually, when the phase step approaches the position $a = -0.94$ (point F in figure 3a), an OV dipole is born in the remote point G of the diffracted beam cross section. Then, the oppositely charged (positive) dipole member rapidly moves against the “main” OV evolution (black curve arrow in figure 3a) and annihilates with the “initial” OV in the point marked by the asterisk (approximately when $a = -0.99$). (This oppositely-charged OV can be called “virtual” [31]: it is “short-living” (exists within a limited range of the phase-step positions a), and its main role is to assist the interaction “transferring” the “main” OV from F to G, which resembles the virtual particles in quantum physics). Simultaneously, the negatively charged dipole member slowly evolves to the right from the point G thus forming the trajectory continuation. These processes are coupled with the rapid transformations of highly anisotropic OVs and are thus difficult for the detailed examination numerically as well as in experiments; for this reason, they were conventionally united into a single event named “jump” [31], and the “moment of jump” was

defined as the value of a at which the new pair of OV is born in point G. Note that in figure 3 the jump is observed only for the red curve and at the closest post-screen distance z because only in this case the jump criterion $|M| > 1$ is realized (see Appendix). In contrast to the case of the edge-diffracted OV beams [29–31], in the red curve of figure 3a the jump occurs at negative a and in the upper half-plane, in full agreement to equations (A14) and (A10).

When $a \rightarrow -\infty$, all the trajectories return to the axis, which is not surprising because the screen becomes again a homogeneous transparency and performs no perturbation to the incident LG beam. Remarkably, for high negative values of a , all the trajectories demonstrate a behavior quite “symmetrical” to that observed when a decreased within the interval $\infty > a > 2$: the trajectories approach the point $(x = 0, y = 0)$ making theoretically infinite number of squeezing spiral coils in the interval $-2 > a > -\infty$ (except for the “degenerate” far field situation in figure 3c). Oppositely to the stage when a decreased, now, when the phase step moves away from the incident beam axis, the spiral wraps clockwise, according to the energy circulation (see figure 1). This agrees with the predictions of the asymptotic model (A13), (A14).

Note also the regular change in the shape of the OV trajectories with growing propagation distance: from the “banana-like” loops carrying distinct reminiscence of the spiral evolution near the coordinate origin (figure 3a for $z = 0.56z_R$) via the “straightened” contours at $z = 1.5z_R$ (figure 3b) towards the “cigar-like” patterns in the far-field (figure 3c). As the far field intensity distribution is always symmetric with respect to the x -axis normal to the diffraction edge (this is a characteristic feature of the far-field diffraction once the incident beam waist coincides with the screen plane [27,30]), the far-field OV trajectories expectedly obey this symmetry. Likewise, it is not surprising that the maximum absolute displacement of the OV is reached when $a = 0$. It is remarkable, however, that all the far-field trajectories form distinct cusps at $a = 0$ (see figure 3c).

3.3. Singular skeleton evolution and topological events caused by the strong phase-step perturbation

When the phase-step value approaches $\varphi = \pi$ (see (2), (3)), the axial OV displacements expectedly become higher but, what is more, the OV trajectory induced by the monotonous screen translation within the range $\infty > a > -\infty$ acquires additional branches and experiences topological reactions. Actually, already the red curve in figure 3a contains some features transient to the strong perturbation behavior which is exhaustively presented in figure 4.

At the initial segment, while $\infty > a > 2$, the axial OV is slightly displaced from the axial position and evolves along the spiral trajectory similarly to what was seen in figure 3 [1,2]. This part of the trajectory is not shown in figure 4a. With further screen translation, while $a < 2$, the OV evolves along the magenta trajectory marked V_1 (see figures 4a and 4b). However, when a reaches $a \approx 1$, an additional pair of OVs is born in the 4th quadrant in point B (this moment is illustrated by the dashed ellipse in figure 2f). The OV V_2 of the same charge as the initial one, moves along the magenta curve while the oppositely charged “accompanying” OV V' (black) moves to the lower beam periphery and eventually disappears (its motion can be numerically traced up to $a \approx 0.3$ but the “far” segment of its trajectory is not shown). So, when the screen position corresponds to $1 > a > 0.4$ (this interval slightly varies with the propagation distance and looks a bit smaller at $z = 1.5z_R$, see figure 4b), the three OVs are present within the central area of the diffracted beam cross section: V_1 , V_2 and V' . With further advance of the screen, $0.4 > a > -0.4$, only two OVs V_1 , V_2 , with the topological charges $m = -1$ (equal the initial one), survive and form the left (V_1) and right (V_2) trajectory branches. Further, when a approaches -0.3 , the oppositely charged OV becomes visible at the upper periphery (V'') and moves to meet V_1 (in figures 4b and 4c, only its part for $a < -0.7$ is shown). V_1 and V'' annihilate at $a \approx -1$ (point A), and for $a < -1$, again, only one OV exists (V_2); with a decreasing further (the phase-step line goes outside the beam cross section), this OV approaches the origin via describing an infinite (theoretically) number of spiral coils, quite similar to the final ($a < -1.5$) segments of the green, blue and red loops in figures 3a and 3b.

The remarkable central symmetry between the trajectories of V_1 and V_2 , V' and V'' is explained by the fact that for $\varphi = \pi$ the phase steps φ and $-\varphi$ are physically equivalent, and condition (7) leads to the intensity profile symmetry

$$|u(x, y, z, a)|^2 = |u(-x, -y, z, -a)|^2.$$

In this context, the clockwise evolution of V_1 at $1 > a > -1$ agrees with the energy circulation handedness and thus follows the general rule noticed for the closed loops observed under the weak-perturbation conditions and $\varphi > 0$ (figure 3). Similarly, the counter-clockwise circulation of V_2 in the region $1 > a > -1$ complies with the same rule for $\varphi < 0$ (see Section 3.2).

The whole pattern acquires the additional mirror symmetry in the far field (figure 4c). The point B moves to the vertical y -axis, and the birth of the OV dipole (V_2, V') occurs exactly in the moment when the OV V_1 approaches this point. During further evolution, V' moves to the far negative- y periphery and leaves the central part of the beam cross section whereas the OVs V_1 and V_2 describe the mirror-symmetric trajectories (note the cusps at $a = 0$ similar to what was observed in the far-field trajectories of simpler curves in figure 3c). At last, approximately at $a = -0.4$, an oppositely charged OV appears at the positive- y periphery (V''), and the annihilation of V_1 and V'' happens in point A, which now lies on the y -axis. Exactly at the moment of annihilation, the vortex V_2 passes the point A, abruptly turns downward and finishes at the coordinate origin.

Alternatively, we can consider how the far-field pattern of figure 4c develops when the observation plane is fixed but the phase step parameter φ approaches the limit value π from below (figure 5). For example, let us focus on the case $\varphi = 3\pi/2$ represented by the red lines (like in figures 3a – 3c). It is seen that while the “main” OV V_1 describes the closed trajectory in the $x < 0$ half-plane (the red “cigar” shown in figure 3c is reproduced in another scale in figure 5), at the moment when $a \approx 0.7$, in the opposite half-plane an OV dipole emerges (in the “red” point B). The “accompanying” dipole member V' goes to the far periphery but its counterpart V_2 regularly evolves along the “gull-wing” trajectory A0B until it vanishes in the annihilation event in the “red” point A (note that this evolution is, generally, opposite to the clock-wise energy circulation). This migration of V_2 is not very noticeable since at any moment V_2 is positioned far from the beam center, in the low-intensity region. At first sight, it looks as one of the multiple OVs emerging in any diffraction pattern formed behind a screen with a sharp inhomogeneity of transmission [26,27] but as we see, the OV V_2 survives up to the far field conditions and behaves as a regular “partner” of the “main” one V_1 .

The association between V_1 and V_2 becomes more evident if we consider the singular skeleton transformation when φ approaches closer to π . For $\varphi = 5\pi/6$, the evolution is very similar but the cyan cigar-like loop in the left half-plane gets larger, the “cyan” points B and A are situated closer to the beam center, and, on the whole, the “cyan” trajectories tend to the symmetric limit case represented by the magenta curves: the cyan loop – from the inside, the “gull-wing” – from the outside. When $\varphi \rightarrow \pi$ still closer, the symmetric structure of figure 4c is formed: points B and A take their places on the vertical axis, and the “cigar” and “gull-wing” curves merge with the “left” and “right” magenta contours, correspondingly. But this reasoning leads to another interpretation of the topological reaction occurring in the “magenta” point A: in contrast to the situation considered in figure 4 (when $\varphi = \pi$ was fixed and the observation plane moved to the far-field zone), now it is reasonable to assume that in point A the OV V_2 annihilates with the V'' whereas the OV V_1 turns downward and continues its motion to the beam center forming thus a closed loop, as is observed for other far-field patterns (cyan and red curves in the left half-plane of figure 5).

Such double interpretation is possible because the far-field situation for $\varphi = \pi$ represents a degenerate case which can be realized by two different limit transitions: $z \rightarrow \infty$ while $\varphi = \pi$ is fixed, and $\varphi \rightarrow \pi$ while $z = \infty$ is fixed. Actually, each of the topological reactions in points B and A involves four OVs on the equal footing. In point B, there is a single input member (“upper” V_1) and three output ones: “left” V_1 , V_2 and V' ; likewise, in point A the three input ones (V_1 , “right” V_2 and

V'') and one output ("lower" OV that moves from A towards the center along the vertical axis) are present. In figure 4c this lower OV was interpreted as a continuation of V_2 , which is compatible with the continuous transition from the patterns presented in figures 4a and 4b. In figure 5, oppositely, treating the "lower OV" as a continuation of V_1 emphasizes the kinship between the magenta curve and the cyan and blue curves.

Analogous of the OVs marked V_2 in figures 4 and 5 exist not only in the far field and not only for $\varphi = \pi$. Generally, presence of the second OV of the same sign as the incident one during a certain part of the transverse phase-step translation is a characteristic feature of the "strong perturbation" conditions. This is illustrated by figure 6 where the phase step $7\pi/8$ is close to the limit value $\varphi = \pi$ and the use of z -dependent, normalized by (9), coordinates enables immediately comparing the OV trajectories at different post-screen distances. It is seen that while V_1 evolves along the closed trajectories (whose shapes gradually change with growing distance z), at a certain, z -dependent, stage of the phase-step translation, its "partner" V_2 emerges in the peripheral area of the 4th quadrant (points B) and migrates across the right-hand part of the beam cross section until it vanishes due to annihilation. (To avoid the figure overloading, the corresponding oppositely charged dipole members accompanying the birth (V') and annihilation (V''), well seen in figures 4 and 5, are omitted in figure 6). The "life times" of the singularities V_2 (seen from the numbers near the initial and final points of their trajectories) depend on z and are limited but, generally, the two OVs, V_1 and V_2 are readily observable when the phase-step is positioned near $a \approx 0$ and are the constitutive components of the diffracted field singular skeleton.

Qualitatively, the pattern of figures 5, 6 is also consistent for the "weak perturbation". For example, each loop in figures 3a and 3b can be considered as a trajectory of V_1 for which the "partner" OV V_2 emerges, migrates and vanishes somewhere at the far right-hand periphery where the light intensity is very low (figure 5 shows that the more the phase step φ differs from π , the farther the corresponding "partner" OV trajectory lies from the beam center). Practically this means that for $\varphi < 2\pi/3$ only the "main" OV V_1 can be well recognized and used for applications while the peripheral "partner" of V_1 , the vortex V_2 , is hardly distinguishable from the "occasional" OVs emerging with the diffraction fringes.

Comparison of figures 6 and 4a discloses additional details of the mechanism of the singular skeleton transformation with growing φ and confirms the deep intrinsic affinity between the "main" V_1 and "partner" V_2 singularities. Indeed, let us consider the red curve of figure 6 describing the situation of $z = 0.56z_R$ and the corresponding figure 4a for $\varphi = \pi$. Obviously, when φ will approach still closer to π , $7\pi/8 < \varphi < \pi$, the jump in the red curve of figure 6 will become still more articulate: the distance between points F and G grows, and the event of the dipole birth in point G takes place at earlier stages of the screen translation (higher values of a). After all, the topological connection between points F and G will be destroyed but the connection between points G and A of the red curves establishes (cf. [31]): V_1 annihilates near the point F with the "accompanying" OV approaching from the upper periphery (V' in Fig. 4a) while the "virtual" member of the dipole born in G moves no longer to F (as was in Fig. 3a) but to the "red" point A that, with $\varphi \rightarrow \pi$, approaches closer to the beam center. As a result, the "red" point F of figure 6 transforms into the point A of figure 4a, whereas the "red" points G and A of figure 6 merge together and form a continuous trajectory interpreted as V_2 in figure 4. Consequently, from a more general point of view, the trajectories of V_1 and V_2 can be considered as separate branches of the certain "combined" path of the migrating singularity, which belongs to a complex multi-sheet abstract surface [41].

4. Conclusion

In this work, we have numerically investigated the localization and migration of OVs in the diffracted optical field obtained after a circular single-charged OV beam passes through the transparent screen with a rectilinear phase step (figure 1). The approach based on the Kirchhoff-Fresnel diffraction theory has shown the interesting and promising possibilities for purposeful

formation of optical fields with desirable and controllable singular structures and revealed additional ways for the physical characterization and diagnostics of the OV beams.

It is demonstrated that a transparent phase-step screen can be an efficient instrument for controlling the OV positions and the whole singular skeleton pattern in the diffracted field. The only input parameters are the phase step value φ that varies within the interval $0 < \varphi < \pi$ and the phase step position a with respect to the incident beam axis that is changed in the course of the transverse screen translation, $\infty > a > -\infty$, across the beam cross section. When the step is situated far from the incident beam center ($|a| \gtrsim 2$ in units of the beam waist radius), the only influence of the phase step is that, in the diffracted field, the OV is slightly shifted from the nominal beam axis. With changing a , the OV evolves along the spiral trajectory, which expectedly unwraps, oppositely to the energy circulation in the incident OV, when the phase step moves towards the axis and wraps back when it moves further to the beam periphery. These spiral trajectories reflect the fundamental helical nature of the incident OV beam and can be used for studying its physical properties and spatial structure.

While the phase step is not very high (“weak perturbation”, $\varphi \lesssim 2\pi/3$), the OV in the diffracted beam describes a smooth closed loop upon the “full” screen translation, $\infty > a > -\infty$. With growing φ , the “strong perturbation” condition is realized so that the continuous evolution of the single OV is replaced by the complicated pattern including trajectories’ discontinuities, jumps and topological reactions with the birth of “new” OVs and annihilation of the “old” ones. The details of the singular skeleton evolution depend on the post-screen propagation distance z but the main qualitative features are preserved up to the far field. In a whole, these findings testify that, by rather simple means, one obtains the ability of forming a well-developed singular skeleton with complicated topological structure which can be efficiently regulated via the change of both parameters a and φ .

The fundamental aspect of the results obtained in this paper is that they provide additional and pictorial demonstrations of the intrinsic helical nature and “hidden” rotational properties of the circular OV beams. Besides, based on the very simple and “palpable” examples, they reveal the fundamental topological features of singular optical fields, the singularities’ evolution, their interactions, topological reactions, etc., which usually requires more complex means (see, e.g., Ref. [42]). Possible applications of the results may be associated with the OV diagnostics; for example, the general view and the direction of the spiral OV evolution at high $|a|$ can be used for detection of the incident OV sign. The sensitivity of the OV position to the phase-step screen parameters may be useful for controllable optical tweezers implementing desirable transportations of the trapped objects. The calculated OV trajectories presented in figures 3 – 5 supply a wide range of helpful facilities: from the very fine regulation available when the OV positions weakly depend on a (for example, near $a = 0$ in curves of figure 3 and 4, and in all situations where $|a| \gtrsim 2$) to the very sensitive conditions near the jumps. In the latter case, a tiny change in the phase-step position with respect to the incident beam axis may induce a considerable shift of the OV core in the diffracted field, which can be applied for the precise detection or measurement of small mechanical displacements and deformations.

Appendix

Here we present some simple analytical expressions describing the OV positions in the vortex LG beam diffracted by a phase step. In this appendix, we consider LG beams with arbitrary topological charge (azimuthal index) m but still require the radial LG mode index to be zero.

The Kirchhoff–Fresnel integral (4) can be recast as

$$u(x, y, z, a) = u^{LG}(x, y, z) + (e^{i\varphi} - 1)Q(x, y, z, a) \quad (\text{A1})$$

where

$$u^{LG}(x, y, z) = \frac{k}{2\pi iz} \int_{-\infty}^{\infty} dy_a \int_{-\infty}^{\infty} dx_a u_a(x_a, y_a) \exp \left\{ \frac{ik}{2z} [(x - x_a)^2 + (y - y_a)^2] \right\} \quad (A2)$$

is the complex amplitude of the unperturbed incident beam (as if it propagated without any screen) and

$$Q(x, y, z, a) = \frac{k}{2\pi iz} \int_{-\infty}^{\infty} dy_a \int_a^{\infty} dx_a u_a(x_a, y_a) \exp \left\{ \frac{ik}{2z} [(x - x_a)^2 + (y - y_a)^2] \right\}. \quad (A3)$$

The screen-induced OV displacements can be found as zeros of function (A1). Under assumption of small perturbation of the incident beam, we suppose that the searched displacements are small compared to the beam waist size b , and then the near-axis approximation of $u^{LG}(x, y, z)$ is valid. In this case, according to equations (A9) and (19) of [29] and (8) of [31],

$$u^{LG}(x, y, z) \simeq \frac{b}{\sqrt{|m|!}} \left(-\frac{iz_R}{b} \right)^{|m|+1} Br^{|m|} \exp(im\phi) \quad (A4)$$

where z_R is determined by (8) and r, ϕ are the polar coordinates in the observation plane ($x = r \cos \phi, y = r \sin \phi$). Further, for $a \gg b$, an asymptotic representation of function (A3) can be derived in the form

$$Q(x, y, z, a) \simeq \frac{b}{\sqrt{|m|!}} \left(-\frac{iz_R}{b} \right)^{|m|+1} Da^{|m|-1} \exp \left(-\frac{a^2}{2b^2} \right) \exp \left[\frac{ik}{z} \left(\frac{a^2}{2} - ax \right) \right] \quad (A5)$$

(see equations (19) and (A8) of [29] and (9) of [31]). The coefficients A and B in (A4) and (A5) are expressed as

$$B = \frac{1}{(z - iz_R)^{|m|+1}}, \quad D = \sqrt{\frac{i}{2\pi}} \frac{k}{z} (-iz_R)^{-|m|-1} \left[k \left(\frac{1}{z} + \frac{i}{z_R} \right) \right]^{-3/2} \quad (A6)$$

(here the relations (20) of [29] are adapted to an LG beam with the waist at the screen plane $z = 0$). Finally, after substitution of (A4) – (A6) into (A1) and equating the result to zero, the polar coordinates of the OV core can be found as

$$r = \left\{ \left| \frac{D(e^{i\phi} - 1)}{B} a^{|m|-1} \exp \left(-\frac{a^2}{2b^2} \right) \right| \right\}^{1/|m|}, \quad (A7)$$

$$\phi + M \cos \phi = \frac{1}{m} \left\{ \arg [D(e^{i\phi} - 1)] - \arg B \right\} + \frac{ka^2}{2mz} + \frac{2N-1}{m} \pi, \quad N = 0, 1, \dots, |m|-1 \quad (A8)$$

where

$$M = \frac{kra}{mz}. \quad (A9)$$

(cf. equations (21) and (22) of [29] and (19), (20) of [31]). In particular, (A8) describes the monotonous growth of r and ϕ with decreasing a (remember that in our case $m = -1$), which explains the spiral-like motion of the OV cores when $|M| < 1$ and possible jumps of the OV trajectories (similar to that visible in the red curve of figure 3a) when $|M| > 1$. According to [31], the jump can occur near positions where

$$\cos \phi = 0, \quad \frac{d}{d\phi} (M \cos \phi) < 0. \quad (A10)$$

In case of the opaque-screen diffraction, for which the described asymptotic model was first derived [29], condition of large negative a was meaningless ($a \ll -b$ meant that the incident beam is almost completely stopped by the screen). Now, for the transparent screen with transmission (2)

and (3), the asymptotic formulas for large negative a also make sense. In this situation, it is suitable to represent the Kirchhoff-Fresnel integral (4) in the form

$$u(x, y, z, a) = \frac{k}{2\pi iz} e^{i\varphi} \left[\int_{-\infty}^{\infty} dy_a \int_{-\infty}^{\infty} dx_a u_a(x_a, y_a) \exp \left\{ \frac{ik}{2z} [(x - x_a)^2 + (y - y_a)^2] \right\} + (e^{-i\varphi} - 1) \int_{-\infty}^{\infty} dy_a \int_{-\infty}^{|a|} dx_a u_a(x_a, y_a) \exp \left\{ \frac{ik}{2z} [(x - x_a)^2 + (y - y_a)^2] \right\} \right] \quad (A11)$$

whence one obtains

$$u(x, y, z, a) = e^{i\varphi} \left[u^{LG}(x, y, z) + (-1)^m (e^{-i\varphi} - 1) Q(-x, -y, z, |a|) \right] \quad (A12)$$

(the signs of the variables are reversed in the second term of (A11), with account that for the LG beams $u_a(-x_a, -y_a) = (-1)^m u_a(x_a, y_a)$). Corresponding analogs of (A7) – (A9) for $a < 0$ acquire the forms

$$r = \left\{ \left| \frac{D(e^{-i\varphi} - 1)}{B} a^{|m|-1} \exp \left(-\frac{a^2}{2b^2} \right) \right| \right\}^{1/|m|}, \quad (A13)$$

$$\phi + M \cos \phi = \frac{1}{m} \left\{ \arg [D(e^{-i\varphi} - 1)] - \arg B \right\} + \frac{ka^2}{2mz} + \frac{2N}{m} \pi - \frac{1 + (-1)^m}{2m} \pi, \quad (A14)$$

(they differ from (A7) – (A9) by replacements $\varphi \rightarrow -\varphi$, $\cos \phi \rightarrow -\cos \phi$, $a \rightarrow |a|$, and the last summand of (A14) appears due to the multiplier $(-1)^m$ in (A12)). According to (A14), the current azimuthal coordinate of the OV core decreases with $a \rightarrow -\infty$ ($d\phi/d(-a) \propto -ka/m < 0$), which explains the clockwise direction of the spirals' wrapping in figures 3a and 3b at large negative a . The “jump conditions” (A10) remain the same but for negative a and $m = -1$ they mean that the jump can occur in the upper half-plane, which exactly corresponds to the jump between points F and G on the red curve of figure 3a.

Acknowledgements

This work was supported, in part, by the Ministry of Education and Science of Ukraine, project 582/18 (State Registration #0118U000198).

References

1. Rubinsztein-Dunlop H et al 2017 Roadmap on structured light *J. Opt.* **19** 013001
2. Soskin M S and Vasnetsov M V 2001 Singular optics *Prog. Opt.* **42** 219–76
3. Bekshaev A Ya, Soskin M S and Vasnetsov M V 2008 *Paraxial Light Beams with Angular Momentum* (New York: Nova Science)
4. Dennis M R, O'Holleran K and Padgett M J 2009 Singular optics: optical vortices and polarization singularities *Prog. Opt.* **53** 293–364
5. Bekshaev A, Bliokh K and Soskin M 2011 Internal flows and energy circulation in light beams *J. Opt.* **13** 053001
6. Chen M, Roux F S and Olivier J C 2007 Detection of phase singularities with a Shack–Hartmann wavefront sensor *J. Opt. Soc. Am. A* **24** 1994–2002
7. Murphy K, Burke D, Devaney N and Dainty C 2010 Experimental detection of optical vortices with a Shack-Hartmann wavefront sensor *Opt. Express* **18** 15448–50
8. Maallo A M S, Almoro P F 2011 Numerical correction of optical vortex using a wrapped phase map analysis algorithm *Opt. Lett.* **36** 1251–3

9. Wang W, Yokozeki T, Ishijima R, Takeda M and Hanson S G 2006 Optical vortex metrology based on the core structures of phase singularities in Laguerre-Gauss transform of a speckle pattern *Opt. Express* **14** 10195–206
10. Anzolin G, Tamburini F, Bianchini A and Barbieri C 2009 Method to measure off-axis displacements based on the analysis of the intensity distribution of a vortex beam *Phys. Rev. A* **79** 033845
11. Cvijetic N, Milione G, Ip E and Wang T 2015 Detecting lateral motion using light's orbital angular momentum *Sci. Rep.* **5** 15422
12. Dennis M R and Götte J B 2012 Topological aberration of optical vortex beams: Determining dielectric interfaces by optical singularity shifts *Phys. Rev. Lett.* **109** 183903
13. Popiołek-Masajada A, Sokolenko B, Augustyniak I, Masajada J, Khoroshun A and Bacia M 2014 Optical vortex scanning in an aperture limited system *Optics and Lasers in Engineering* **55** 105–12
14. Cojoc D, Garbin V, Ferrari E, Businaro L, Romanato F and Di Fabrizio E 2005 Laser trapping and micro-manipulation using optical vortices *Microelectronic Engineering* **78** 125–31
15. Nieminen T A, Higuett J, Knoner G, Loke V L Y, Parkin S, Singer W, Heckenberg N R and Rubinsztein-Dunlop H 2006 Optically driven micromachines: progress and prospects, *Proc. SPIE* **6038** 237–45
16. Dholakia K, Reece P and Gu M 2008 Optical micromanipulation *Chemical Society Reviews* **37** 42–55
17. Padgett M and Bowman R 2011 Tweezers with a twist *Nature Photonics* **5** 343–8
18. Gibson G, Courtial J, Padgett M, Vasnetsov M, Pas'ko V, Barnett S and Franke-Arnold S 2004 Free-space information transfer using light beams carrying orbital angular momentum *Opt. Express* **12** 5448–56
19. Wang J, Yang J-Y, Fazal I M, Ahmed N, Yan Y, Huang H, Ren Y, Yue Y, Dolinar S, Tur M and Willner A E 2012 Terabit free-space data transmission employing orbital angular momentum multiplexing *Nature Photonics* **6** 488–96
20. Khoroshun A, Chernykh A, Kirichenko J, Ryazantsev O and Bekshaev A 2017 Singular skeleton of a Laguerre–Gaussian beam transformed by the double-phase-ramp converter *Applied Optics* **56** 3428–34
21. Vasnetsov M V, Marienko I G and Soskin M S 2000 Self-reconstruction of an optical vortex *JETP Lett.* **71** 130–3
22. Gorshkov V N, Kononenko A N and Soskin M S 2001 Diffraction and self-restoration of a severe screened vortex beam *Proc. SPIE* **4403** 127–37
23. Masajada J 2000 Gaussian beams with optical vortex of charge 2- and 3-diffraction by a half-plane and slit *Optica Applicata* **30** 248–56
24. Masajada J 2000 Half-plane diffraction in the case of Gaussian beams containing an optical vortex *Opt. Commun.* **175** 289–94
25. Cui H X, Wang X L, Gu B, Li Y N, Chen J and Wang H T 2012 Angular diffraction of an optical vortex induced by the Gouy phase *J. Opt.* **14** 055707
26. Bekshaev A Ya, Mohammed K A and Kurka I A 2014 Transverse energy circulation and the edge diffraction of an optical-vortex beam *Appl. Opt.* **53** B27–37
27. Bekshaev A Ya and Mohammed K A 2015 Spatial profile and singularities of the edge-diffracted beam with a multicharged optical vortex *Opt. Commun.* **341** 284–94
28. Chernykh A, Bekshaev A, Khoroshun A, Mikhaylovskaya L, Akhmerov A and Mohammed K A 2015 Edge diffraction of optical-vortex beams formed by means of the “fork” hologram *Proc. SPIE* **9809** 980902
29. Bekshaev A, Chernykh A, Khoroshun A and Mikhaylovskaya L 2016 Localization and migration of phase singularities in the edge-diffracted optical-vortex beams *J. Opt.* **18** 024011

30. Bekshaev A, Chernykh A, Khoroshun A and Mikhaylovskaya L 2017 Displacements and evolution of optical vortices in edge-diffracted Laguerre-Gaussian beams *J. Opt.* **19** 055605
31. Bekshaev A, Chernykh A, Khoroshun A and Mikhaylovskaya L 2017 Singular skeleton evolution and topological reactions in edge-diffracted circular optical-vortex beams *Opt. Commun.* **397** 72–83
32. Khoroshun A, Chernykh O, Tatarchenko H, Sato S, Kozawa Y, Popiolek-Masajada A, Szatkowski M and Lamperska W 2019 Chain of optical vortices synthesized by a Gaussian beam and the double-phase-ramp converter *OSA Continuum* **2** 320–31
33. Fu S, Wang T, Gao Y and Gao C 2016 Diagnostics of the topological charge of optical vortex by a phase-diffractive element *Chinese Optics Letters* **14** 080501
34. Bekshaev A Ya and Orlinska O V 2010 Transformation of optical vortex beams by holograms with embedded phase singularity *Opt. Commun.* **283** 1244–50
36. Bekshaev A Ya and Sviridova S V 2010 Effects of misalignments in the optical vortex transformation performed by holograms with embedded phase singularity *Opt. Commun.* **283** 4866–76
37. Khoroshun A N, Gorshkov V N and Soskin M S 2002 Evolution of a singular beam perturbed by the amplitude or phase transparency with rectilinear edge *Visnik of the Volodymyr Dahl East Ukrainian National University* No 12(58) part 2 117–128 (in Russian)
38. Masajada J, Leniec M, Drobczynski S, Thienpont H and Kress B 2009 Micro-step localization using double charge optical vortex interferometer *Opt. Express* **17** 16144–159
39. Masajada J, Leniec M, Jankowska E, Thienpont H, Ottevaere H and Gomes V 2008 Deep microstructure topography characterization with optical vortex interferometer *Opt. Express* **16** 19179–91
40. Born M and Wolf E 1999 *Principles of Optics* (Cambridge: University Press)
41. Solimeno S, Crosignani B and DiPorto P 1986 *Guiding, Diffraction and Confinement of Optical Radiation* (Orlando: Academic Press)
40. Soskin M and Vasil'ev V 2014 Topological singular chain reactions in dynamic speckle fields *J. Opt. Soc. Am. B* **31** A56–A61
41. Farkas H M and Kra I 1980 *Riemann Surfaces (2nd ed.)*, (Berlin, New York: Springer-Verlag)

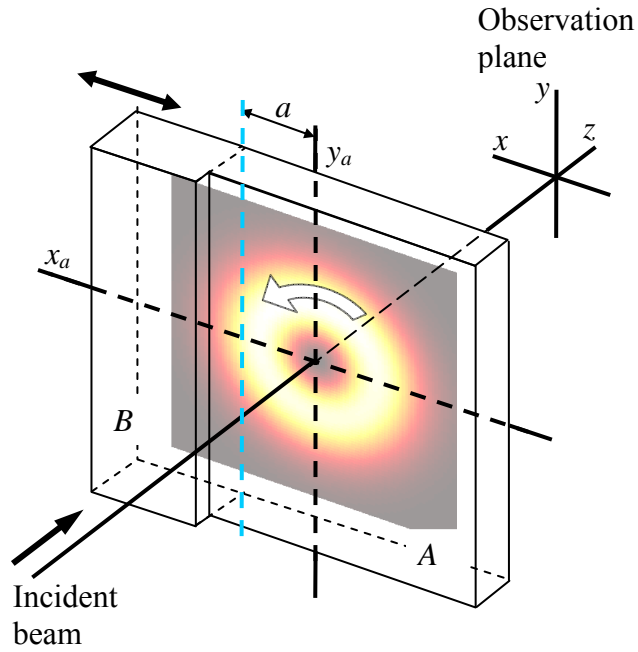


Figure 1. Scheme of the OV transformation by the transparent screen with rectilinear phase step. The screen is orthogonal to the incident beam axis z and is placed in the transverse plane $z = 0$; the boundary between the two screen parts introducing different phase shifts is parallel to axis y ; the arrow shows the transverse energy circulation in the incident OV beam. After the transformation performed in the plane $z = 0$, the beam structure is registered (e.g., by the CCD camera) in the observation plane positioned at a distance z behind the screen. Further explanations see in text.

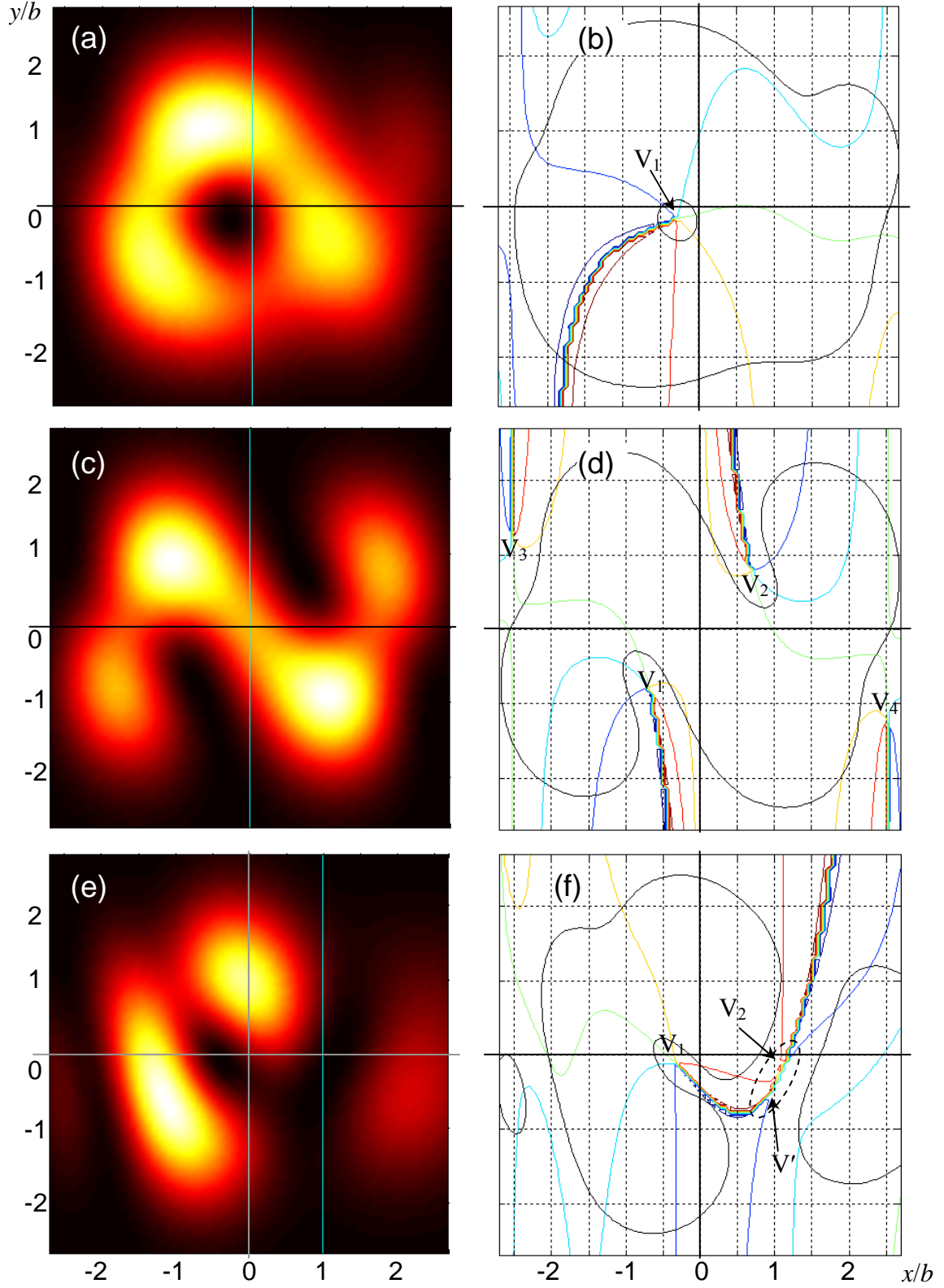
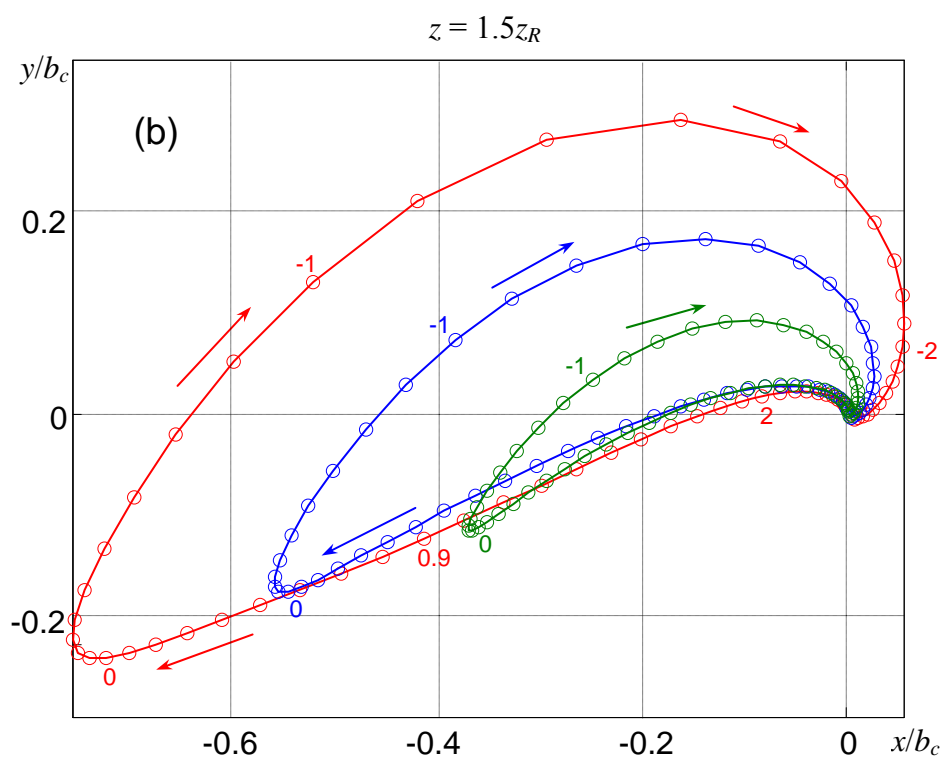
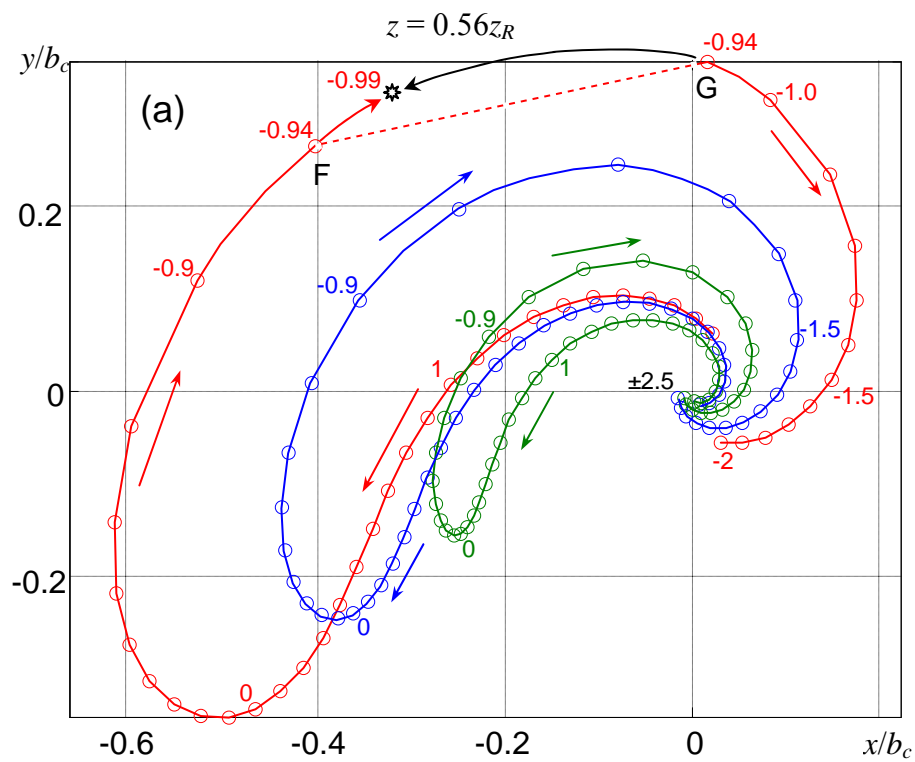


Figure 2. (a, c, e) Intensity and (b, d, f) phase profiles of the diffracted $LG_{0,-1}$ beam at a distance $z = 0.557z_R$ behind the screen with the phase step (a, b) $\varphi = \pi/3$ ($A = 1$, $B = 0.5 + 0.866i$) and (c – f) $\varphi = \pi$ ($A = 1$, $B = -1$). The step position a (see figure 1) is denoted by the vertical light-blue lines in panels (a, c, e) and equals to $a = 0$ in (a – d) and $a = 1$ in (e, f) (in units of b). Black contours in panels (b, d, f) indicate the intensity level 0.1 of the maximum, dashed ellipse in panel (f) shows the area where a pair of OV's is being formed (corresponds to the vicinity of the point B in figure 4a).



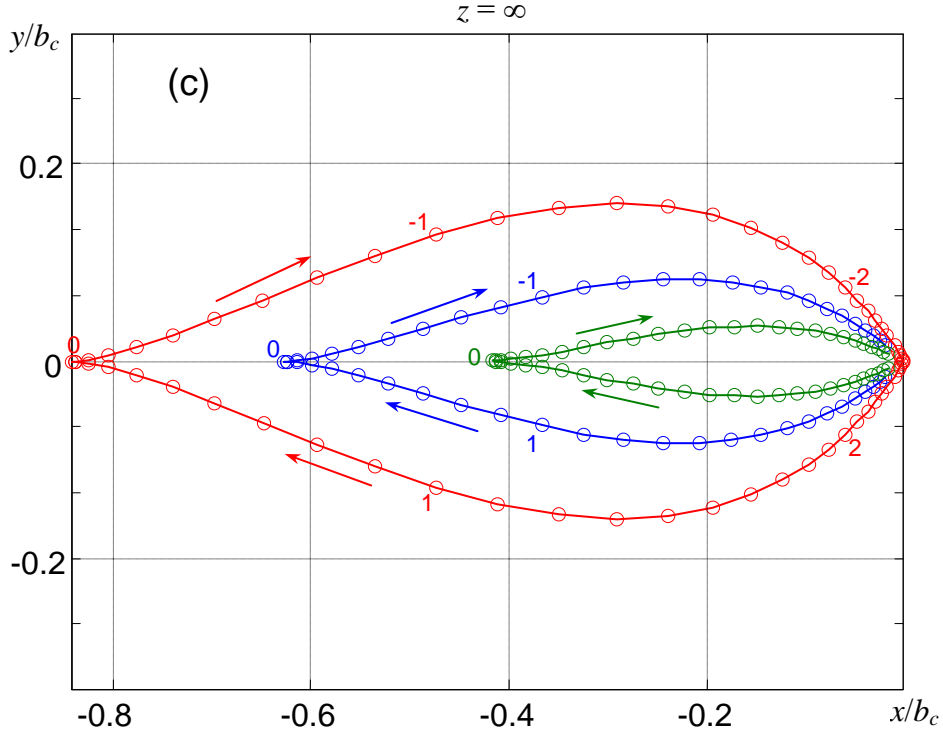


Figure 3. Migration of the OVs in the observation planes distanced from the screen by (a) $z = 0.56z_R$, (b) $z = 1.5z_R$ and (c) $z \rightarrow \infty$ (far field). Green, blue and red curves describe the cases $\varphi = \pi/3$, $\varphi = \pi/2$ and $\varphi = 2\pi/3$, correspondingly; markers indicate the current values of a multiple of 0.1 in units of b , some values of a are indicated explicitly near the markers; arrows show the direction of the OV motion when the screen translates in the negative x direction (a changes from ∞ to $-\infty$, see figure 1). Black line in panel (a) shows the trajectory of the “virtual” OV participating in the jump process shown by the dotted segment, asterisk marks the point of annihilation (explanations in text); transverse coordinates are expressed in units of the current Gaussian envelope radius (9).

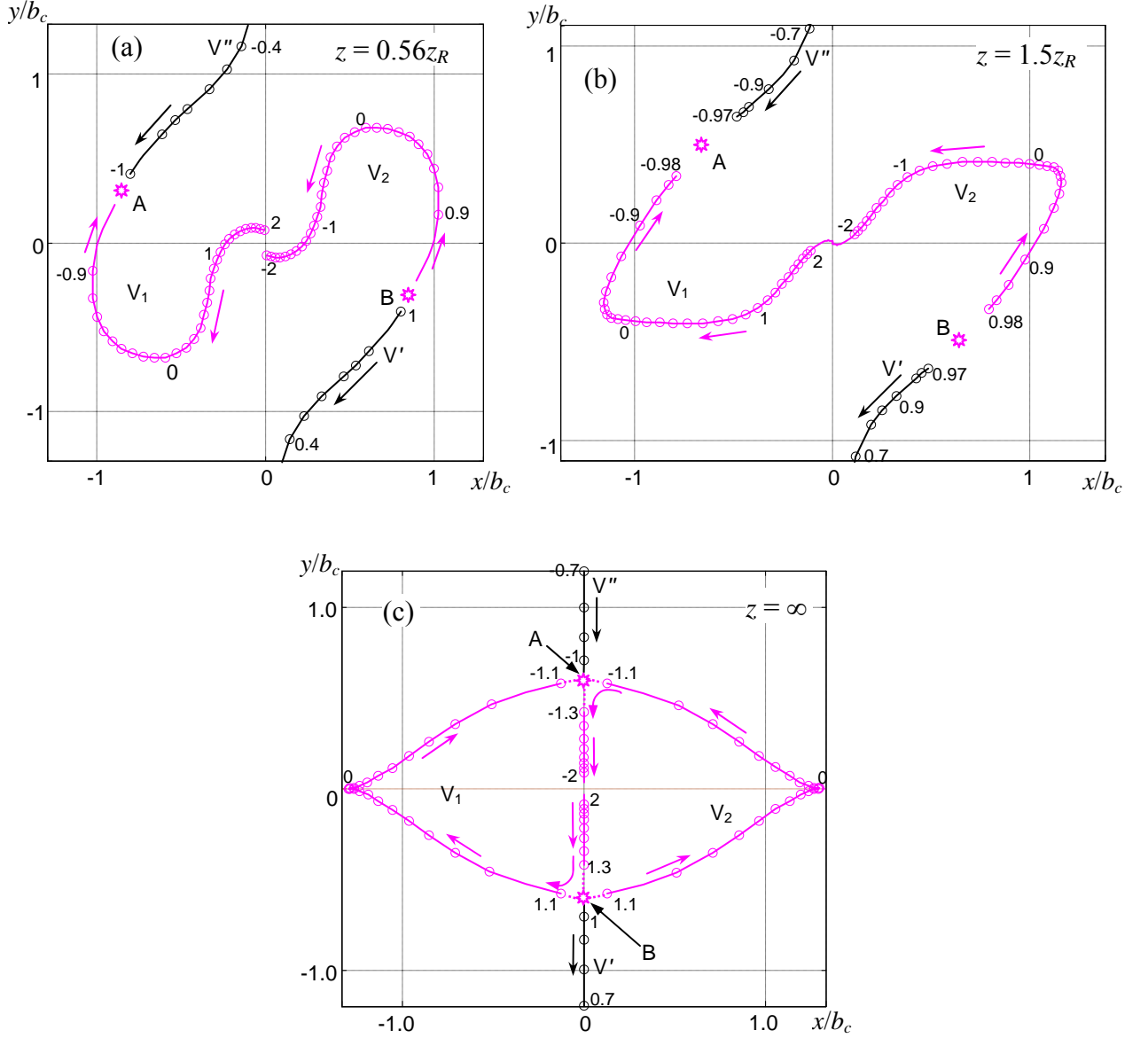


Figure 4. Migration of the OV within the diffracted beam cross section when the transparent screen with the phase step $\varphi = \pi$ (see (2) and (3)) is translated in the negative x direction (a changes from ∞ to $-\infty$, see figure 1), for (a) $z = 0.56z_R$, (b) $z = 1.5z_R$ and (c) $z \rightarrow \infty$ (far field). Magenta curves show trajectories of the “main” near-axial OVs, black lines are the trajectories of the oppositely charged “accompanying” OVs participating in the topological reactions with the “main” ones. Arrows show the direction of the OV motion; markers indicate the current values of a multiple of 0.1 in units of b , some values of a are indicated explicitly near the markers, asterisks show the points of topological reactions. Transverse coordinates are expressed in units of (9).

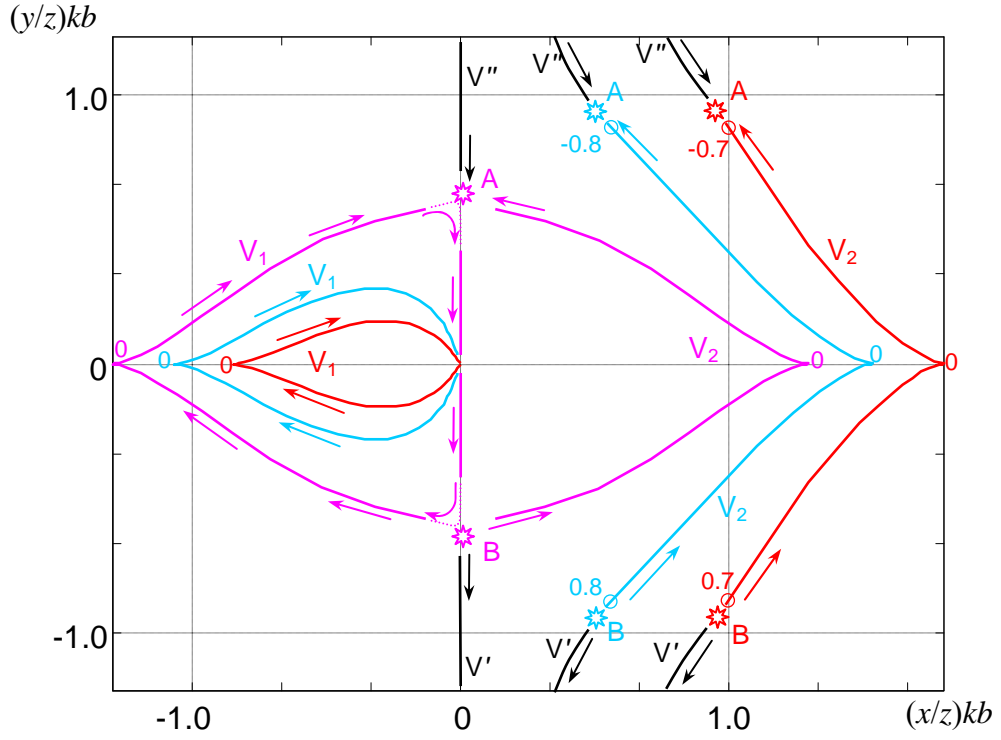


Figure 5. OV trajectories in the far-field observation plane ($z \rightarrow \infty$) corresponding to the screen translation from $a = \infty$ to $a = -\infty$ (see figure 1) for the phase step values: (red curves) $\varphi = 2\pi/3$, (cyan curves) $\varphi = 5\pi/6$ and (magenta curves) $\varphi = \pi$. Asterisks denote the points of topological reactions, black lines are the trajectories of the oppositely charged “accompanying” OVs participating in the topological reactions, arrows show the directions of the OV migration, transverse coordinates are expressed in units of (9), which are equivalent to the far-field angular coordinates in units of the Gaussian envelope divergence $(kb)^{-1}$.

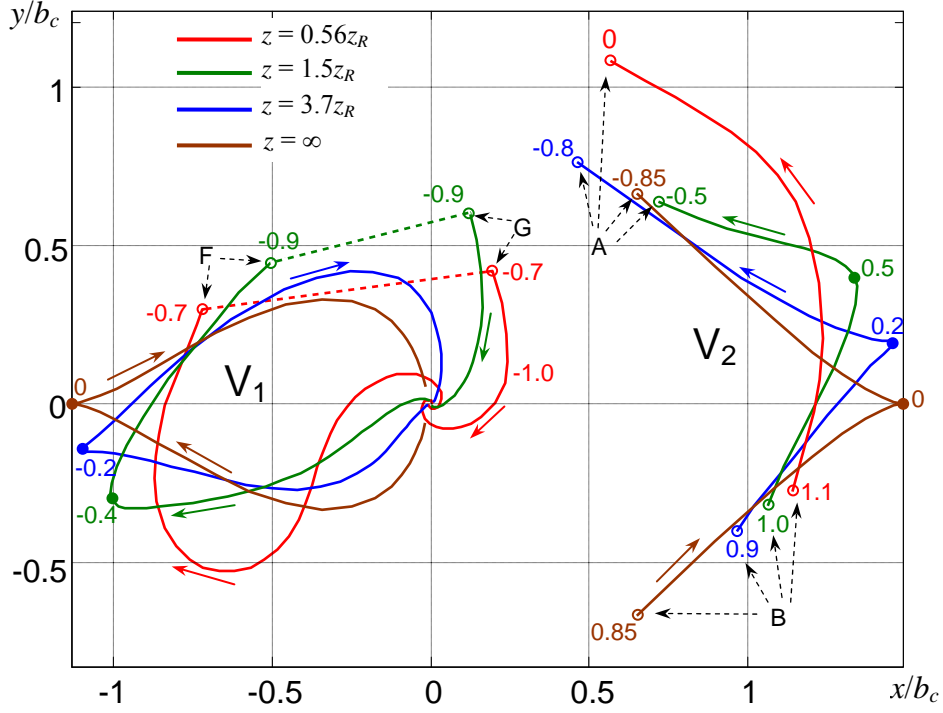


Figure 6. Trajectories of the “main” OV₁ (in the region $x/b_c < 0.3$) and their “partners” V₂ (at $x/b_c > 0.3$) in the observation planes distanced from the screen by (red) $z = 0.56z_R$, (green) $z = 1.5z_R$, (blue) $z = 3.7z_R$ and (brown) in the far-field ($z \rightarrow \infty$) for the phase step value $\varphi = 7\pi/8$. Arrows show the OV motion when the phase-step screen translates from $a = \infty$ to $a = -\infty$ (see figure 1); the transverse coordinates are expressed in the normalized units of (9). Filled circles mark the trajectories’ “vertices” (return points); empty circles denote the starting F and final G points of jumps (shown by dotted lines for V₁, cf. figure 3a) and points where the OV_s V₂ emerge (are born) B and vanish (annihilate) A; trajectories of their “accompanying” counterparts V’ and V’’ (see figures 4, 5) are not shown. Numbers near markers indicate corresponding values of the phase-step position a (see figure 1). The jumps in the V₁ trajectories exist only at $z = 0.56z_R$ and $z = 1.5z_R$ (the corresponding paths of “virtual” OV_s – analogs of the black segment in figure 3a – are omitted) and disappear at larger distances. It is visible how the trajectories of V₁ and V₂ gradually transform with growing z to the symmetric far-field forms depicted in brown (cf. figures 3c, 4c and 5).